



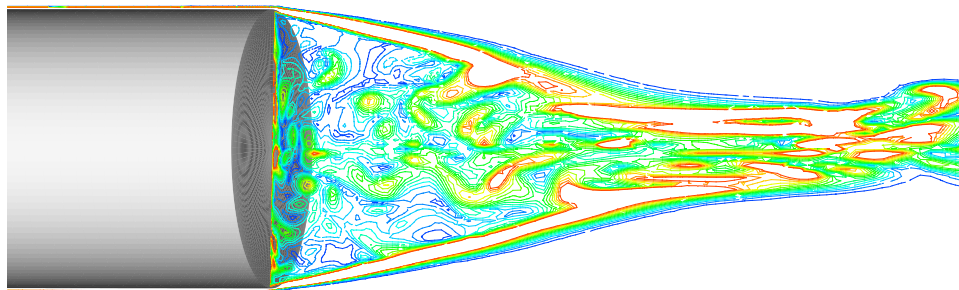
AIAA 02-0586

**Detached-Eddy Simulation with
Compressibility Corrections Applied
to a Supersonic Axisymmetric Base
Flow**

James R. Forsythe
*Department of Aeronautics
United States Air Force Academy*

Klaus A. Hoffmann
*Department of Aerospace Engineering
Wichita State University*

Kyle D. Squires
*Department of Mechanical Engineering
Arizona State University*



**40th AIAA Aerospace Sciences
Meeting and Exhibit
14-17 January 2002 / Reno, Nevada**

Detached-Eddy Simulation with Compressibility Corrections Applied to a Supersonic Axisymmetric Base Flow

James R. Forsythe*
*Department of Aeronautics
United States Air Force Academy*

Klaus A. Hoffmann†
*Department of Aerospace Engineering
Wichita State University*

Kyle D. Squires‡
*Department of Mechanical Engineering
Arizona State University*

Detached-Eddy Simulation proposed by Spalart, Jou, Strelets, and Allmaras, is applied to an axisymmetric base flow at supersonic conditions. Detached-Eddy Simulation is a hybrid approach to modeling turbulence that combines the best features of the Reynolds-averaged Navier-Stokes and Large Eddy Simulation approaches. In its Reynolds-averaged mode, it is currently based on either the Spalart-Allmaras turbulence model or Menter's Shear Stress Transport model. In its Large Eddy Simulation mode, it is based on the Smagorinski sub-grid scale model. The intended application of Detached-Eddy Simulation is the treatment of massively separated, high-Reynolds number flows over complex configurations (entire aircraft, automobiles, etc.). Because of its intended use for complex configurations, an unstructured grid solver Cobalt is used. The current work incorporates compressible shear layer corrections in both the Spalart-Allmaras based and Shear Stress Transport based DES models. The effect of these corrections on both DES and RANS models is examined. Comparisons are made to the experiments of Herrin and Dutton. Solutions are made on several grids – both structured and unstructured – to test the sensitivity of the models and code to grid refinement and grid type.

Introduction

THERE are various techniques for the numerical prediction of turbulent flows. These range from Reynolds-averaged Navier-Stokes, to Large Eddy Simulation, to Direct Numerical Simulation. Direct numerical simulation (DNS) attempts to resolve **all** scales of turbulence. Because DNS must model the scales from the largest to the smallest, the grid resolution requirements are very high, and increase drastically with Reynolds number. Large eddy simulation (LES) attempts to model the smaller, more homogeneous scales, while resolving the larger, energy containing scales. This makes LES's grid requirements less than those for DNS. To accurately resolve the boundary layer, however, LES must accurately resolve the energy containing eddies in the boundary

layer, which requires very small streamwise grid spacing. The Reynolds-averaged Navier-Stokes approach (RANS) attempts to solve for the time-averaged flow. This means that all scales of turbulence must be modeled. Since the large scales for separated flows are very dependent on the geometry, RANS models often fail to provide accurate results for these flows. RANS models, however, can provide accurate results for attached boundary layer flows with minimal grid spacing requirements. Spalart [1] provides a discussion of these various techniques.

These techniques have very different computational requirements. Spalart et al. [2] estimated the computational cost for an LES computation of a whole aircraft. Their conclusion was that LES over a full aircraft would not be possible for over 45 years. Their estimate led to the formulation of Detached-Eddy Simulation, which attempts to combine the advantages of LES and RANS into one model. The idea is that RANS is used in the boundary layer, where it performs well, with much lower grid requirements than

* Assistant Professor, Member AIAA

† Professor, Associate Fellow AIAA

‡ Professor, Associate Fellow AIAA

This paper is a work of the U.S. Government and is not subject to copyright protection in the United States. 2002

LES. LES is then used in the separated regions. Shur et al. [3] calibrated the model for isotropic turbulence, and applied it to a NACA 0012 section. The model agreed well with lift and drag predictions to 90 degrees angle of attack. Consantinescu and Squires [4] applied Detached-Eddy Simulation to the turbulent flow over a sphere at several of Reynolds numbers. Issues of grid resolution, numerical accuracy, and values of the model constant were examined. The model was compared to Large Eddy Simulation and Reynolds-averaged models. Travin et al. [5] applied DES to a circular cylinder at sub- and super- critical Reynolds number, and obtained a grid converged solution that agreed well with experiments. Strelets [6] presents numerous cases using DES: cylinder, airfoil, backstep, triangle in a channel, raised runway section, and a landing gear. Although some cases showed very little improvement over RANS, none performed worse than RANS, and many performed far better.

Forsythe et al. [7] performed DES on the supersonic axisymmetric base flow of Herrin and Dutton [8, 9] using an unstructured solver. Good solutions were obtained only by dropping the DES constant. This paper is an attempt to improve upon these preliminary results. A larger selection of grids is used to further examine the sensitivity of the model to grid refinement. SST based DES is used for the first time on this flow. Both RANS models and DES models are run with and without compressibility corrections.

Flow Description / Experimental and Computational Studies

An important form of separation found in supersonic flowfields is base flow separation. This kind of flow is commonly found behind such objects as missiles, rockets, and projectiles. The low pressure found behind the base causes base drag which can be a sizable portion of the total drag. To make computational fluid dynamics useful as a design tool, it is important to be able to predict this base pressure accurately with computational methods.

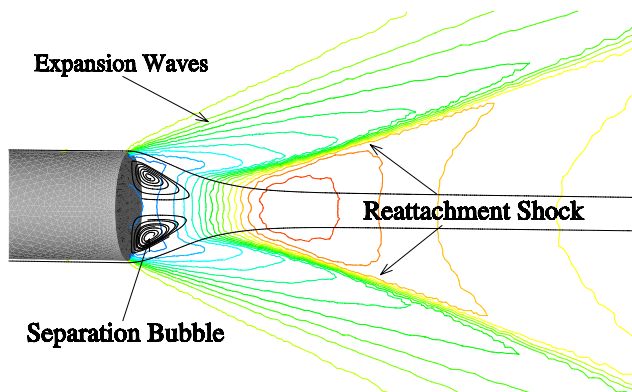


Fig. 1 Axisymmetric Base Flow — Expansion and Shock Waves

A schematic of an axisymmetric base flow is shown

in Figure 1, with pressure contours and streamlines. The large turning angle behind the base causes separation, and a region of reverse flow to form — the separation bubble. The size of the separation bubble determines the turn angle of the flow coming off the back of the base, and therefore the strength of the expansion waves. A smaller separation bubble causes the flow to turn sharply, leading to a stronger expansion wave, and lower pressures behind the base. Therefore, small separated regions cause larger base drag than large regions.

Directly behind the base, in the separation bubble, the reverse flow can be seen. The point along the axis of symmetry where the streamwise velocity is zero, is considered to be the shear layer reattachment point. The further this point is from the base, the larger the separation bubble is, and the higher you would expect the base pressure to be. As the shear layer reattaches, the flow is forced to turn along the axis of symmetry. This turning of the flow, causes a reattachment shock to be formed, as seen in Figure 1.

Figure 1 shows the time average of the flowfield. For high Reynolds numbers, the incoming boundary layer and the flow behind the base will be turbulent, leading to highly unsteady flow behind the base. Bourdon et al. [10] present planar visualizations of the large-scale turbulent structures in axisymmetric supersonic base flows.

Dutton et al. [11] provides a good overview on the progress on computing high-speed separated base flows. Several complicating factors in modeling this flow are presented:

1. The shear layer exists under highly compressible conditions, i.e. at high convective Mach numbers.
2. The shear layer encounters a strong adverse pressure gradient at reattachment
3. The expansion wave at the base corner influence the the initial turbulence structure of the shear layer
4. Strong streamline curvature at the reattachment point
5. The enclosed recirculating region imposes a highly energetic and nonuniform reverse velocity at the inner edge of the shear layer

Goebel and Dutton [12] and Clemens and Mungal [13] show that the turbulent structure in the shear layer is altered by the compressible conditions, compared to the incompressible case.

Early attempts to predict base flows are summarized by Delery and Lacau [14], and include the Chapman-Korst component method, and the viscid-inviscid integral interaction technique of Crocco and Lees. “However, solution of the full, Reynolds-averaged Navier-Stokes equations using currently available numerical

methods offers the ability to more realistically predict the details of the base flowfield structure, i.e., to remove many of the assumptions inherent in the component and integral techniques.” [11] Also, more complex geometries require a more general approach such as solving the RANS equations.

Attempts to solve afterbody flows with the RANS approach has been ongoing since the late 1970s. Putnam and Bissinger [15] summarize these early attempts and conclude that the current (mid 1984) methods were unable to accurately predict the pressures after separation. They also recommended that “the assessment criteria of numerical predictions should be based on the surface pressure distributions and flowfield characteristics and not simply on the overall afterbody drag.” Petrie and Walker [16] tested the predictive capabilities of RANS calculations by soliciting solutions from a number of groups for a power-on base flow configuration, for which they had experimental data. The experimental data was not released to the groups performing the calculations. Many fundamental parameters such as the base pressure magnitude and radial variation and recirculation region size were not accurately predicted with large variations among the different groups.

More recently, several groups have obtained results with much better agreement, including Benay et al. [17], Caruso and Childs [18], Childs and Caruso [19, 20], Peace [21], Tucker and Shyy [22], Suzen et al. [23], Forsythe et al. [26]. Factors that affected the accuracy of the RANS simulation of these flows included

1. Solution-adapted grid alignment in the high gradient shear layer regions
2. Improved Turbulence modeling
 - (a) modeling the effects of compressibility
 - (b) modeling the effects of streamline curvature

Childs and Caruso [19] also suggested that “comparison of simply the base pressure between computation and experiment, without any complementary flowfield data, can lead to false conclusions regarding the accuracy of the numerical solutions, due to cancellation of errors caused by inaccurate turbulence modeling and insufficient grid resolution.”

Dutton et al. [11] state that “the difficult problem of turbulence modeling is the most critical outstanding issue in the accurate RANS predictions of these complex flows.” Since Herrin and Dutton [9] published their detailed experimental results on a $M=2.46$ axisymmetric supersonic base flow, several researchers have performed RANS computations on this flow, attempting to find an accurate RANS turbulence model. Sahu [24] used two algebraic turbulence models (Baldwin-Lomax and Chow) and Chien’s low Reynolds number $k-\epsilon$ model. Chuang and Chieng [25] published

results for three higher-order models: Chien’s two equation $k-\epsilon$ model, a two-layer algebraic stress model, and Shima’s Reynolds stress model. Tucker and Shyy [22] used several variations of two-equation $k-\epsilon$ models, including the original Jones-Launder formulation, and extensions to allow improved response to the means strain rate and compressibility effects. Both Sahu’s $k-\epsilon$ computation and Chuang and Chieng’s Reynolds stress prediction of the base pressure was in reasonable agreement with the experiments. However all of the models poorly predicted the mean velocity and turbulence fields. Also, even though all three studies employed a “standard” $k-\epsilon$ model, they obtained substantially different predictions of the base pressure distribution. This points to possible dependence on numerical implementation, grid resolution, turbulence model implementation and boundary conditions. Suzen et al. [23] tested several popular RANS models on a 2D base, and obtained good agreement for base pressure by adding compressibility corrections to Menter’s model. Forsythe et al. [26] applied several RANS models to the 2D and axisymmetric base. Although the 2D base pressure was well predicted by two equation models with compressibility corrections, no model predicted the flat pressure profile for the axisymmetric base.

Based on the unsatisfactory results of RANS calculations so far, other approaches such as Large Eddy Simulation or Direct Numerical Simulation should be considered. Dutton et al. [11] states that “In order to avoid the difficulties inherent in turbulence modeling for the Reynolds-averaged Navier-Stokes (RANS) approach, the Large Eddy Simulation (LES) or Direct Numerical Simulations (DNS) techniques will eventually be applied to high-speed flows.” Harris and Fasel [27] performed DNS on a $M=2.46$ two-dimensional base flow with the goal of addressing “the nature of the instabilities in such wake flows and to examine the structures that arise from these instabilities.” Fureby, Nilsson and Andersson [28] performed large eddy simulation on the axisymmetric $M=2.46$ base flow of Mathur and Dutton [35], Herrin and Dutton [9], including the effects of base bleed. Subgrid scale models used were the Monotone Integrated LES (MILES) model, the one-equation eddy-viscosity model, and the Smagorinski model. In general, agreements to experiment were quite good. However the size of the recirculation region was slightly under-predicted. A potential source of error cited was the approaching boundary layer thickness in the computations was smaller than experimental. This is presumably because the grid resolution in the boundary layer was inadequate for an LES computation, although the grid was not shown.

Forsythe et al. [7] applied Detached-Eddy Simulation on the supersonic axisymmetric base flow using an unstructured solver. The boundary layer was treated entirely by RANS which was able to adequately pre-

dict the boundary layer thickness prior to separation. Two grids were used, with the coarse grid being clearly inadequate. The fine grid gave a DES solution that agreed quite well with experiments if the DES model constant was dropped enough. Although the good agreement with the experiments was encouraging, the lack of a grid refined solution and the need to adjust the DES constant kept the results from being conclusive. Additionally, the poor performance of the Spalart-Allmaras RANS model on this flow created skepticism on the part of the author that the Spalart-Allmaras model was a good base for a hybrid model for this flow. Menter's models and Wilcox's $k-\omega$ model performed far better than the Spalart-Allmaras model, especially when compressibility corrections were included.

Baurle et al. [29] later explored hybrid RANS/LES for the supersonic axisymmetric base flow. A boundary layer code was run prior to the base to obtain a fully turbulent velocity profile of the correct thickness just prior to the base. Then a Monotone Integrated Large Eddy Simulation (MILES) was performed in the base region. This approach allowed the authors to examine numerical issues apart from modeling issues since a pure LES approach was used behind the base. The agreement with experiments was quite good.

The current paper is an attempt to resolve many of the issues revealed in the previous study [7] in order to build confidence in DES for compressible flows. Four grids (both structured and unstructured) are used to examine the sensitivity of the DES model to grid refinement and grid type. DES based on Menter's Shear Stress Transport model is applied to determine the sensitivity of DES on the RANS model for this flow. Compressibility corrections are applied to both Spalart-Allmaras and Shear Stress Transport based DES. Comparisons are made to LES and RANS solutions.

Governing Equations/Flow Solver

The unstructured flow solver Cobalt was chosen because of its speed and accuracy. Cobalt is a commercial version of Cobalt₆₀. The relevant improvements in the commercial version for this study were the inclusion of SST based DES, faster per-iteration times, ability to calculate time-averages and turbulent statistics, an improved spatial operator, and improved temporal integration. Strang et al. [30] validated the code on a number of problems, including the Spalart-Allmaras model (which forms the core of the DES model). Tomaro et al. [31] converted Cobalt₆₀ from explicit to implicit, enabling CFL numbers as high as one million. Grismer et al. [32] then parallelized the code, yielding a linear speedup on as many as 1024 processors. Forsythe et al. [26] provided a comprehensive testing/validation of the RANS models: Spalart-Allmaras, Wilcox $k-\omega$, and Menter's models

Parallel METIS domain decomposition library of Karypis and Kumar [33], Karypis et al. [34] is incorporated in Cobalt. ParMetis divides the grid into nearly equally sized zones that are then distributed one per processor.

The Navier-Stokes equations are solved in an inertial reference frame. The primitive variables can be seen as either being time averaged or spatially averaged depending on whether Detached-Eddy Simulation is operating in a Reynolds-averaged mode or Large Eddy Simulation mode. In integral form, the Navier-Stokes equations are:

$$\begin{aligned} \frac{\partial}{\partial t} \iiint_{\mathcal{V}} Q dV + \iint_{\mathcal{S}} (f\hat{i} + g\hat{j} + h\hat{k}) \cdot \hat{n} dS \\ = \iint_{\mathcal{S}} (r\hat{i} + s\hat{j} + t\hat{k}) \cdot \hat{n} dS \end{aligned}$$

where:

$$Q = \begin{bmatrix} \rho \\ \rho u \\ \rho v \\ \rho w \\ \rho e \end{bmatrix} \quad f = \begin{bmatrix} \rho u \\ \rho u^2 + p \\ \rho uv \\ \rho vw \\ u(\rho e + p) \end{bmatrix} \quad (1)$$

$$g = \begin{bmatrix} \rho v \\ \rho uv \\ \rho v^2 + p \\ \rho vw \\ v(\rho e + p) \end{bmatrix} \quad h = \begin{bmatrix} \rho w \\ \rho vw \\ \rho w^2 + p \\ w(\rho e + p) \end{bmatrix} \quad (2)$$

$$r = \begin{bmatrix} 0 \\ \tau_{xx} \\ \tau_{xy} \\ \tau_{xz} \\ a \end{bmatrix} \quad s = \begin{bmatrix} 0 \\ \tau_{xy} \\ \tau_{yy} \\ \tau_{yz} \\ b \end{bmatrix} \quad t = \begin{bmatrix} 0 \\ \tau_{xz} \\ \tau_{yz} \\ \tau_{zz} \\ c \end{bmatrix}$$

Here $a = u\tau_{xx} + v\tau_{xy} + w\tau_{xz} + kT_x$, $b = u\tau_{xy} + v\tau_{yy} + w\tau_{yz} + kT_y$, and $c = u\tau_{xz} + v\tau_{yz} + w\tau_{zz} + kT_z$; \mathcal{V} is the fluid element volume; \mathcal{S} is the fluid element surface area; \hat{n} is the outward-pointing unit normal to \mathcal{S} ; \hat{i} , \hat{j} , and \hat{k} are the Cartesian unit vectors; ρ is the density; p is the pressure; u , v , and w are the velocity components; e is the specific energy per unit volume; T is the temperature; k is the thermal conductivity; and τ_{xx} , τ_{yy} , τ_{zz} , τ_{xy} , τ_{xz} , and τ_{yz} are the viscous stress tensor components. The ideal gas law closes the system of equations and the entire equation set is non-dimensionalized by freestream density and speed of sound.

The semi-discrete form of the equations is:

$$\begin{aligned} \mathcal{V}_i \frac{dQ_i}{dt} + \sum_{M=1}^{N_i} (f^M \hat{i} + g^M \hat{j} + h^M \hat{k}) \cdot \hat{n}^M \mathcal{S}^M \\ = \sum_{M=1}^{N_i} (r^M \hat{i} + s^M \hat{j} + t^M \hat{k}) \cdot \hat{n}^M \mathcal{S}^M \end{aligned}$$

where the subscripted i and superscripted M denote quantities for the i^{th} cell and the M^{th} face of cell i , respectively, and N_i is the number of faces bounding cell i .

To model the effects of turbulence, a turbulent viscosity (μ_t) is provided by the turbulence model. To obtain k_t , a turbulent Prandtl number is assumed (0.9) with the following relation: $Pr_t = \frac{c_p \mu_t}{k_t}$. In the governing equations, μ is replaced by $(\mu + \mu_t)$ and k is replaced by $(k + k_t)$.

Spalart-Allmaras Model

The Spalart-Allmaras (SA) one-equation model [36] solves a single partial differential equation for a variable $\tilde{\nu}$ which is related to the turbulent viscosity. The differential equation is derived by “using empiricism and arguments of dimensional analysis, Galilean invariance and selected dependence on the molecular viscosity.” The model includes a wall destruction term that reduces the turbulent viscosity in the log layer and laminar sublayer and trip terms that provides a smooth transition from laminar to turbulent. For the current research, the trip term was turned off.

$$\frac{D\tilde{\nu}}{Dt} = c_{b1}\tilde{S}\tilde{\nu} - c_{w1}f_w \left[\frac{\tilde{\nu}}{d} \right]^2 + \frac{1}{\sigma} \left[\nabla \cdot ((\nu + \tilde{\nu}) \nabla \tilde{\nu}) + c_{b2} (\nabla \tilde{\nu})^2 \right] \quad (3)$$

The turbulent viscosity is determined by

$$\nu_t = \tilde{\nu} f_{v1} \quad f_{v1} = \frac{\chi^3}{\chi^3 + c_{v1}^3} \quad \chi \equiv \frac{\tilde{\nu}}{\nu} \quad (4)$$

S is the magnitude of the vorticity, and the modified vorticity is:

$$\tilde{S} \equiv S + \frac{\tilde{\nu}}{\kappa^2 d^2} f_{v2} \quad f_{v2} = 1 - \frac{\chi}{1 + \chi f_{v1}} \quad (5)$$

where d is the distance to the closest wall. The wall destruction function, f_w , is:

$$f_w = g \left[\frac{1 + c_{w3}^6}{g^6 + c_{w3}^6} \right]^{\frac{1}{6}} \quad (6)$$

$$g = r + c_{w2}(r^6 - r) \quad r \equiv \frac{\tilde{\nu}}{S \kappa^2 d^2} \quad (7)$$

The closure coefficients are given by:

$$\begin{aligned} c_{b1} &= 0.1355 & \sigma &= \frac{2}{3} & c_{b2} &= 0.622 \\ \kappa &= 0.41 & c_{w1} &= \frac{c_{b1}}{\kappa^2} + \frac{(1+c_{b2})}{\sigma} & c_{w2} &= 0.3 \\ c_{w3} &= 2 & c_{v1} &= 7.1 & & \end{aligned} \quad (8)$$

Compressibility Corrections

Spalart [37] suggested the use of the compressibility correction of Secundov [38]. The following destruction term is added to right-hand-side of Equation 3

$$-C_5 \tilde{\nu}^2 U_{i,j} U_{i,j} / a^2 \quad (9)$$

where a is the speed of sound, and empirically $C_5 = 3.5$. The term accounts for the reduced spreading rates in a compressible shear layer by reducing the turbulent eddy viscosity. Cases run with the compressibility correction active are denoted by "CC".

Menter's Shear Stress Transport Model

Wilcox's $k-\omega$ model is well behaved in the near wall region, where low Reynolds number corrections are not required. However, it is generally sensitive to the freestream values of ω . On the other hand, the $k-\epsilon$ equations are relatively insensitive to freestream values, but behave poorly in the near wall region [39]. This sensitivity seems to be a factor mainly for free shear flows, and does not seem to adversely affect boundary layer flows.

Menter [40, 41, 42] proposed a combined $k-\epsilon$, $k-\omega$ model which uses the best features of each model. The model uses a parameter F_1 to switch from $k-\omega$ to $k-\epsilon$ in the wake region to prevent the model from being sensitive to freestream conditions. The governing differential equations are:

$$\frac{D}{Dt} (\rho k) = \tau_{ij} \frac{\partial u_i}{\partial x_j} - \beta^* \rho \omega k \quad (10)$$

$$+ \frac{\partial}{\partial x_j} \left[(\mu + \sigma_k \mu_t) \frac{\partial k}{\partial x_j} \right]$$

$$\frac{D}{Dt} (\rho \omega) = \frac{\gamma \rho}{\mu_t} \tau_{ij} \frac{\partial u_i}{\partial x_j} - \beta \rho \omega^2 \quad (11)$$

$$+ \frac{\partial}{\partial x_j} \left[(\mu + \sigma_\omega \mu_t) \frac{\partial \omega}{\partial x_j} \right] + 2\rho (1 - F_1) \sigma_{\omega 2} \frac{1}{\omega} \frac{\partial k}{\partial x_j} \frac{\partial \omega}{\partial x_j}$$

To compute the switching function F_1 :

$$\arg_1 = \min \left(\max \left(\frac{\sqrt{k}}{0.09 \omega y}, \frac{500 \mu}{\rho \omega y^2} \right); \frac{4 \rho \sigma_{\omega 2} k}{CD_{k\omega} y^2} \right) \quad (12)$$

$$CD_{k\omega} = \max \left[2\rho \sigma_{\omega 2} \frac{1}{\omega} \frac{\partial k}{\partial x_i} \frac{\partial \omega}{\partial x_i}; 10^{-20} \right] \quad (13)$$

$$F_1 = \tanh(\arg_1^4) \quad (14)$$

The switching function also determines the value of the model constants. If ϕ_1 represents a generic constant of the $k-\omega$ equations, and ϕ_2 represents the same

constant for the k- ϵ equations, then the model constants used in Equations 10 and 11 are determined by:

$$\phi = F_1 \phi_1 + (1 - F_1) \phi_2 \quad (15)$$

The model limits the turbulent shear stress to $\rho a_1 k$ where $a_1 = 0.31$. The turbulent viscosity is given by:

$$\mu_t = \frac{\rho a_1 k}{\max(a_1 \omega; \Omega F_2)} \quad (16)$$

where Ω is the absolute value of vorticity. The function F_2 is included to prevent singular behavior in the freestream where Ω goes to zero. F_2 is given by:

$$F_2 = \tanh(\arg_2^2)$$

$$\arg_2 = \max\left(2 \frac{\sqrt{k}}{0.09 \omega y}; \frac{400 \nu}{y^2 \omega}\right)$$

The model constants are shown in Table 1.

Set 1 (k- ω)

$\sigma_{k1} = 0.85$	$\sigma_{\omega 1} = 0.5$	$\beta_1 = 0.0750$
$\beta^* = 0.09$	$\kappa = 0.41$	$\gamma_1 = \frac{\beta_1}{\beta^*} - \frac{\sigma_{\omega 1} \kappa^2}{\sqrt{\beta^*}}$

Set 2 (k- ϵ)

$\sigma_{k2} = 1.0$	$\sigma_{\omega 2} = 0.856$	$\beta_1 = 0.0828$
$\beta^* = 0.09$	$\kappa = 0.41$	$\gamma_2 = \frac{\beta_2}{\beta^*} - \frac{\sigma_{\omega 2} \kappa^2}{\sqrt{\beta^*}}$

Table 1 Menter's Shear Stress Transport model coefficients

Compressibility Correction

Menter did not include compressibility corrections in his model. Suzen and Hoffmann [43], however, added compressible dissipation and pressure dilatation terms to the k- ϵ portion of Menter's models. When Menter's blending process is applied, the following equations result:

$$\begin{aligned} \frac{D}{Dt}(\rho k) &= \tau_{ij} \frac{\partial u_i}{\partial x_j} + (1 - F_1) \overline{p'' d''} \\ &- \beta^* \rho \omega k (1 + \alpha_1 M_t^2 (1 - F_1)) \\ &+ \frac{\partial}{\partial x_j} \left[(\mu + \sigma_k \mu_t) \frac{\partial k}{\partial x_j} \right] \end{aligned}$$

$$\begin{aligned} \frac{D}{Dt}(\rho \omega) &= \frac{\gamma \rho}{\mu_t} \tau_{ij} \frac{\partial u_i}{\partial x_j} + (1 - F_1) \beta^* \alpha_1 M_t^2 \rho \omega^2 \\ &+ \frac{\partial}{\partial x_j} \left[(\mu + \sigma_\omega \mu_t) \frac{\partial \omega}{\partial x_j} \right] - \beta \rho \omega^2 \\ &+ 2 \rho (1 - F_1) \sigma_{\omega 2} \frac{1}{\omega} \frac{\partial k}{\partial s x_j} \frac{\partial \omega}{\partial x_j} \\ &- (1 - F_1) \frac{\overline{p'' d''}}{\nu_t} \end{aligned}$$

where the pressure dilatation term is:

$$\overline{p'' d''} = -\alpha_2 \tau_{ij} \frac{\partial u_i}{\partial x_j} M_t^2 + \alpha_3 \rho \epsilon M_t^2 \quad (17)$$

and the closure coefficients for the compressible corrections are:

$$\alpha_1 = 1.0 \quad \alpha_2 = 0.4 \quad \alpha_3 = 0.2$$

By adding these corrections only to the k- ϵ portions of the model, the near wall solution (k- ω portion) is unaffected, as observed by Forsythe et al. [44]. Cases run with the compressibility correction active are denoted by "CC".

Detached-Eddy Simulation

Detached-Eddy Simulation was proposed by Spalart et al. [2]. The motivation for this approach was to combine the best features of Large Eddy Simulation with the best features of the Reynolds-averaged Navier-Stokes approach. RANS tends to be able to predict attached flows very well with a low computation cost. LES, on the other hand, has a high computation cost, but can predict separated flows more accurately.

The model was originally based on the Spalart-Allmaras one equation RANS turbulence model detailed above and in [36]. The wall destruction term is proportional to $(\tilde{\nu}/d)^2$, where d is the distance to the closest wall. When this term is balanced with the production term, the eddy viscosity becomes: $\tilde{\nu} \propto S d^2$, where S is the local strain rate. The Smagorinski LES model varies its Sub-Grid-Scale (SGS) turbulent viscosity with the local strain rate, and the grid spacing: Δ , i.e. $\nu_{SGS} \propto S \Delta^2$. If, therefore, d is replaced by Δ in the wall destruction term, the S-A model will act as a Smagorinski LES model.

To exhibit both RANS and LES behavior, d in the SA model is replaced by

$$\tilde{d} = \min(d, C_{DES} \Delta) \quad (18)$$

When $d \ll \Delta$, the model acts as a RANS model. When $d \gg \Delta$, the model acts as a Smagorinski LES model. Therefore the model can be "switched" to LES mode by locally refining the grid. In an attached boundary layer, a RANS simulation will have highly stretched grids in the streamwise direction. To retain RANS behavior in this case Δ is taken as the largest spacing of any direction ($\Delta = \max(\Delta x, \Delta y, \Delta z)$). The model was calibrated by Shur et al. [3] using isotropic turbulence to give C_{DES} of 0.65. Although C_{DES} was reduced previously [7], the current study uses 0.65 for all cases.

Strelets [6] introduced a DES model based on Menter's Shear Stress Transport model. In the SST model, the turbulent length scale is given by $l_{k-\omega} = k^{1/2}/(\beta^* \omega)$. The DES modification replaces the length scale by $\tilde{l} = \min(l_{k-\omega}, C_{DES} \Delta)$ in the dissipative

term of the k-transport equation. I.e. the dissipation term is $D_{DES}^k = \rho k^{3/2} / \tilde{l}$. Since the compressibility corrections outlined above are designed to decrease the turbulence length scale, it was decided to include them in the equation for \tilde{l} , i.e. $l_{k-\omega} = k^{1/2} / (\beta^* (1 + \alpha_1 M_t^2 (1 - F_1)) \omega)$. Since Menter's SST is based on a blending of $k - \epsilon$ and $k - \omega$, Strelets [6] calibrated the model by running both the $k - \epsilon$ and $k - \omega$ DES models on isotropic turbulence. This led to $C_{DES}^{k-\epsilon} = 0.61$ and $C_{DES}^{k-\omega} = 0.78$. The traditional blending function was used to blend between the two constants - i.e. $C_{DES} = (1 - F_1)C_{DES}^{k-\epsilon} + F_1C_{DES}^{k-\omega}$. The recommended constants were used in the current study.

Cobalt accepts arbitrary cell types. For the current study a combination of tetrahedrons and prisms were used. This is in contrast to structured grids, which use hexahedral cells. Prisms were used in the boundary layer, to reduce the number of cells needed, and to increase the accuracy of the boundary layer computation by increasing the orthogonality of the cells. Previously, Forsythe et al. [7] used the longest edge in each cell as Δ . However it was pointed out that a tetrahedron with an edge length equal to a hexahedral will have roughly 1/6 the volume (imagine a cube cut into 6 tetrahedra). A more consistent method of defining the length scale is used in the current study - the longest distance between the cell center, and all the neighboring cell centers. Since Cobalt is cell-centered, this definition provides a length scale based on the distance between neighboring degrees of freedom.

In the current study, the streamwise and spanwise grid spacing was slightly larger than the boundary layer thickness, ensuring that the model was operating in a RANS mode in the boundary layer (since $d < \Delta$ in the boundary layer).

Results

Test Conditions

The experimental conditions for the axisymmetric base of Herrin and Dutton [8] were matched in the current computations. Freestream conditions of $M=2.46$ and a unit Reynolds number of 45 million per meter were imposed as inflow. With a base radius of 31.75mm, the resulting Reynolds number based on the diameter was $2.858 \cdot 10^6$. The outflow was supersonic, so simple extrapolation was used as an outflow condition. The test conditions are summarized in Table 2.

Grids

Two unstructured grids and two structured grids were used in the current study to examine the effects of grid resolution and grid type. All grids used a cylinder of length $8R$, where R is the base radius. This length was determined by running Wilcox's boundary layer code - EDDYBL [45] with the Spalart-Allmaras

M_∞	2.46
ρ_∞	$0.7549 \frac{kg}{m^3}$
p_∞	$3.1415 \cdot 10^4 \frac{N}{m^2}$
T_∞	145K
Re	$\frac{45 \cdot 10^6}{m}$
R	31.75mm
$U_\infty = U_0$	$593.8 \frac{m}{sec}$

Table 2 Test Conditions for the axisymmetric base flow

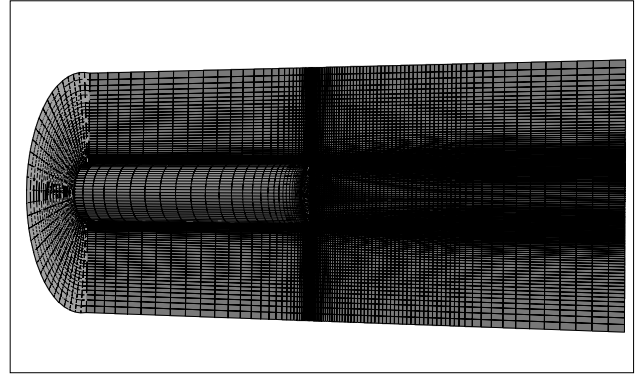


Fig. 2 Coarse structured grid (SGC) - 330,000 cells

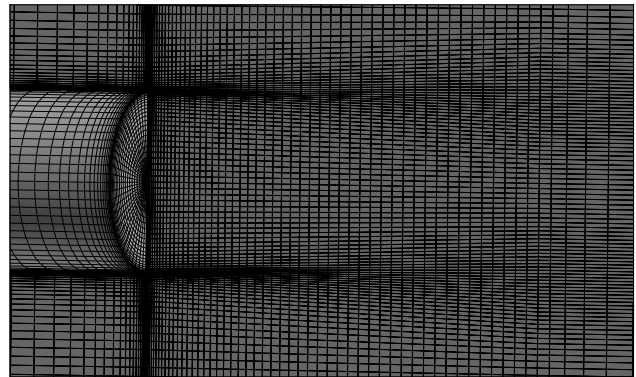


Fig. 3 Coarse structured grid (SGC) closeup - 330,000 cells

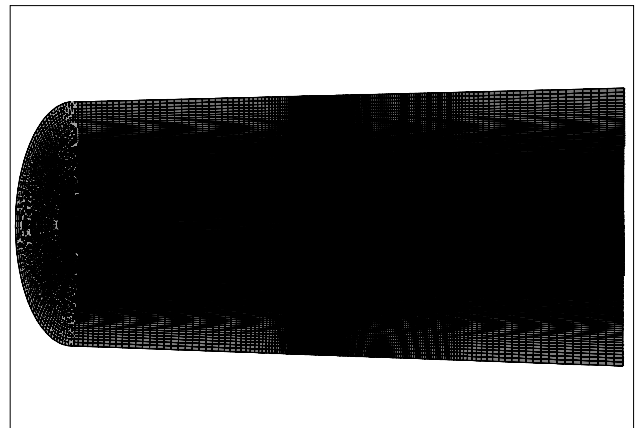


Fig. 4 Fine structured grid (SGF) - 2.60×10^6 cells

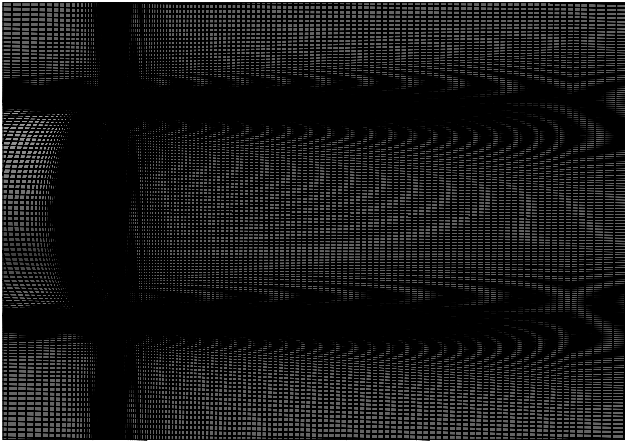


Fig. 5 Fine structured grid (SGF) closeup – 2.60×10^6 cells

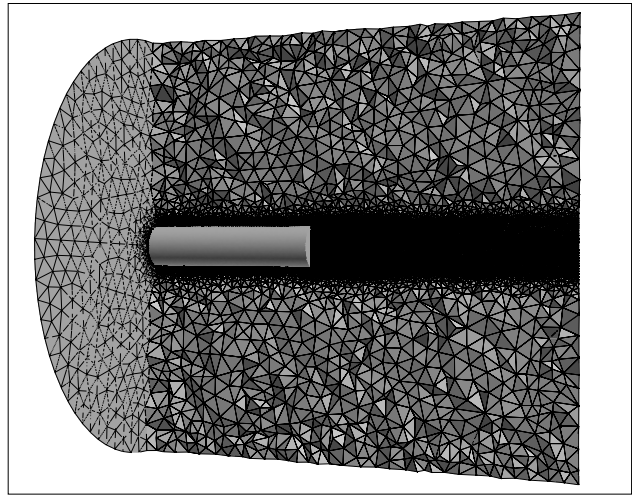


Fig. 8 Gridgen grid (GG) – 2.75×10^6 cells

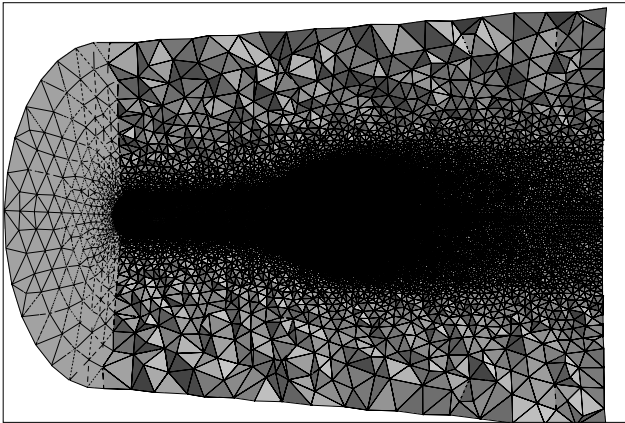


Fig. 6 VGRIDns grid (VG) - 2.86×10^6 cells

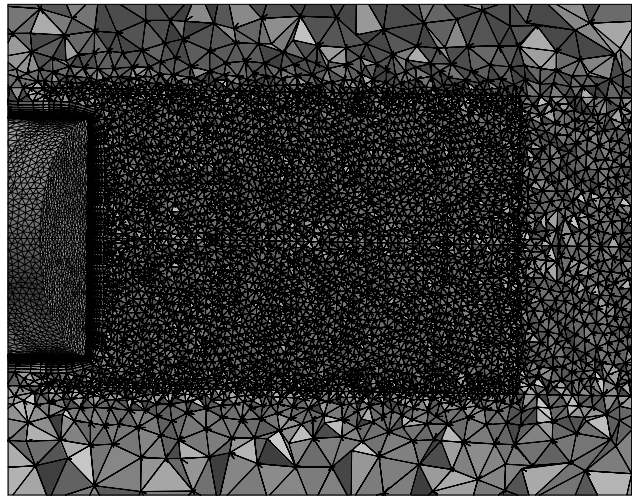


Fig. 9 Gridgen grid (GG) closeup – 2.75×10^6 cells

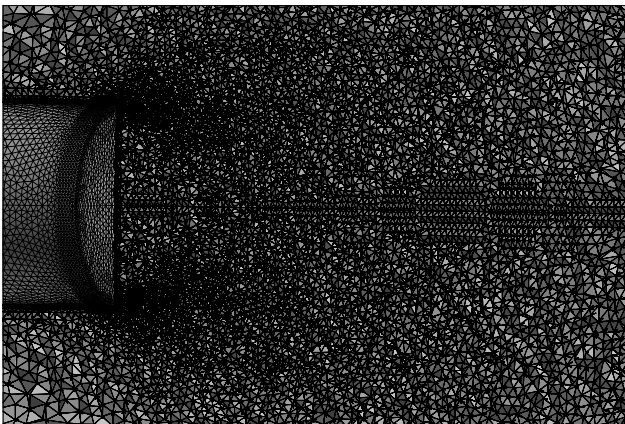


Fig. 7 VGRIDns grid (VG) closeup – 2.86×10^6 cells

model, to see what length was needed to match the experimental momentum thickness.

The two structured grids were provided by Baurle et al. [29], and are shown in Figures 2 through 5. The provided grids contained only a short portion upstream of the base, so an additional set of points was added to extend the cylinder upstream to 8R. Two grids were used, with the fine grid having twice as many points in each coordinate direction. The grid densities of the coarse and fine grids were 330,000 and 2.60×10^6 respectively. The average first y^+ for the coarse grid on a Spalart-Allmaras calculation was 14, while the fine grid was half that value. This is well above the recommended value of 1 [37]. Since Baurle et al. [29] were using a separate boundary layer code to calculate the boundary layer profile prior to the base, this spacing was adequate. In the current study, however, the boundary layer was treated with RANS, so the resolution was inadequate. The outflow was placed 10R downstream, while the farfield boundary was at 4.15R from the axis of symmetry. The structured coarse and fine grids are denoted by SGC and SGF respectively.

The two unstructured grids had the same basic dimensions as each other. The outflow boundary was placed 12R downstream. The experimental wind tunnel walls were modeled as a slip boundary at 10R from the axis of symmetry. The first unstructured grid, pictured in Figures 6 and 7 was created using VGRIDns [46], and was used for previous computations [7]. Although VGRIDns is a pure tetrahedral grid generator, a Cobalt utility *blacksmith* was used to recombine the tetrahedra in the boundary layer into prisms. The average first y^+ spacing was 0.7 for the Spalart-Allmaras model. Cells were concentrated in the shear layer and in the separated region. The grid consisted of 2.86×10^6 cells, and is denoted by VG.

The second unstructured grid was created with Gridgen [47], and is pictured in Figures 8 and 9. This grid was created using the concepts in the "Young-Person's Guide to Detached-Eddy Simulation Grids" [48]. Gridgen's multiblock unstructured gridding capability was used to pack points in the separated region (or focus region) to give better LES resolution. Approximately half of the 2.75×10^6 cells were in a region that extended 4R downstream, and 1.3R from the axis of symmetry. The boundary layer consisted of prisms, with an average first y^+ spacing of less than 0.2 for the Spalart-Allmaras model. This grid is denoted by GG.

Calculation Details

A timestep study was performed previously [7]. Pressure was monitored at ten locations along the axis of symmetry, and the timestep varied. Also, two full DES calculations were done with a timestep that varied by a factor of two, with little effect on the mean flow. The current calculations reduced the timestep from 5.0×10^{-6} in the previous study to 3.2×10^{-6} . This gives a non-dimensional timestep (by base diameter and freestream velocity) of 0.025. In the base region, the velocities are far lower than the freestream velocity, leading to local CFL numbers that are less than one outside the boundary layer. The other parameters used for the temporal integration were two Newton sub-iterations, 32 matrix sweeps, and a temporal damping of 0.025 (inviscid) and 0.01 (viscous). The calculations were run for 4000 iterations prior to beginning to take time averages. Then statistics were calculated internally by Cobalt for minimum 10,000 iterations. The code was run second order in both time and space. RANS calculation were done with a CFL of 1×10^6 to obtain a steady state solution rapidly. Previous runs suggested that the RANS calculations would not give an unsteady solution.

As in the previous study, asymmetries were observed in the mean flow. In the previous study, only 4000 total iterations were used to calculate time averages. The current study showed that these asymmetries were greatly reduced but not eliminated by running as many

	SGC	SGF	VG	GG
SA			X	
SA-CC			X	
SST			X	
SST-CC			X	
MILES	X	X		X
DES-SA	X	X	X	X
DES-SA-CC	X		X	X
DES-SST			X	X
DES_SST-CC			X	X

Table 3 Test Matrix

as 40,000 iterations. This many iterations was considered impracticable, so instead averages were taken both in time, and in the azimuthal direction.

Calculations were performed on an IBM SP3 and a Linux cluster. Between 32 to 256 processors were used. With 256 processors, the most expensive calculations (14,000 iterations, 2.85×10^6 , DES-SST model) took around 30 wall clock hours. The steady state calculations took about a tenth that time, since less than 2,000 iterations were necessary with less subiterations.

The test matrix for the turbulence models and the different grids is shown in Table 3. All of the RANS runs were performed on the VGRIDns grid, since RANS calculations on that grid were shown previously to match well with a more fine 2D structured grid (see [26] and [7]).

RANS Results

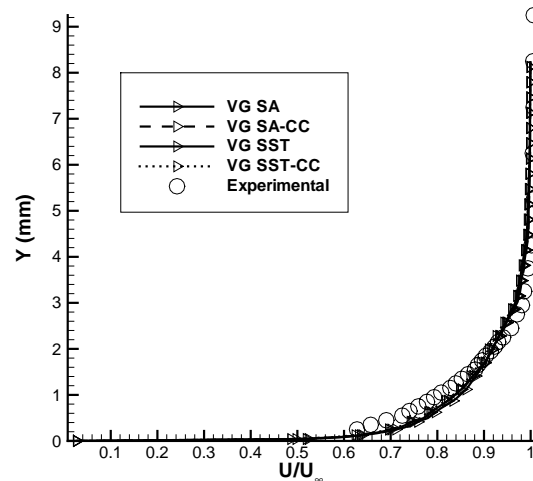


Fig. 10 Boundary layer profile 1mm prior to the base – RANS models

Figures 10 through 18 show results for the Spalart-Allmaras and Menter's Shear Stress Transport RANS models on the VGRIDns grid. As seen in Figure 10 both models, with and without the compressibility corrections match the boundary layer thickness prior to the base quite well. The shape of the velocity pro-

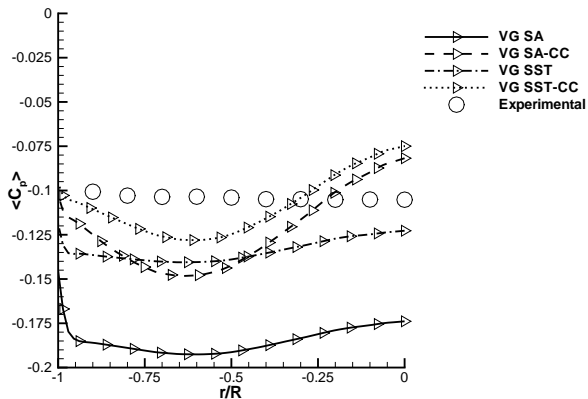


Fig. 11 Pressure along the base – RANS models

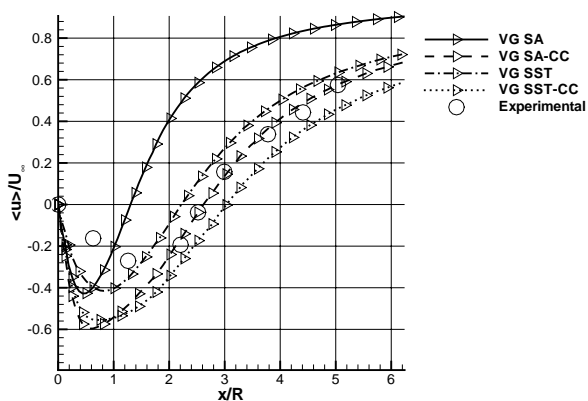


Fig. 12 Centerline velocity – RANS models

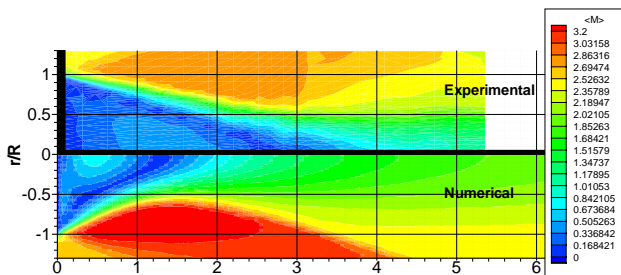


Fig. 13 Mach contours behind the base – Spalart-Allmaras on VGRIDns grid vs. Experiments

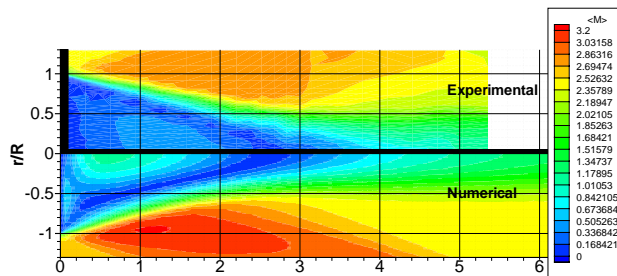


Fig. 14 Mach contours behind the base – Spalart-Allmaras with compressibility corrections on VGRIDns grid vs. Experiments

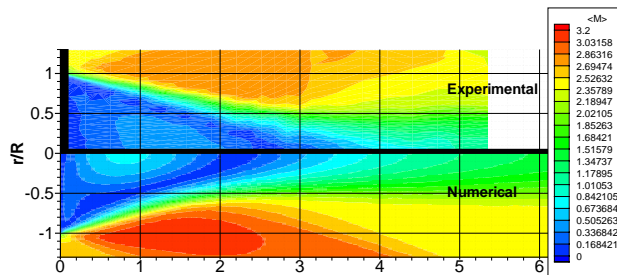


Fig. 15 Mach contours behind the base – Shear Stress Transport on VGRIDns grid vs. Experiments

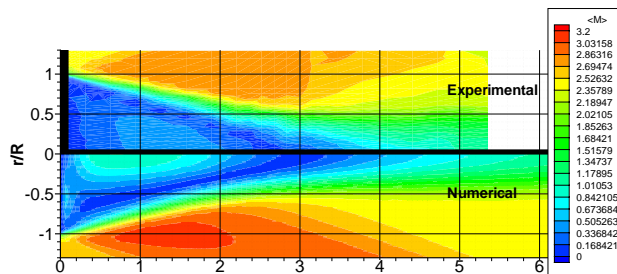


Fig. 16 Mach contours behind the base – Shear Stress Transport with compressibility corrections on VGRIDns grid vs. Experiments

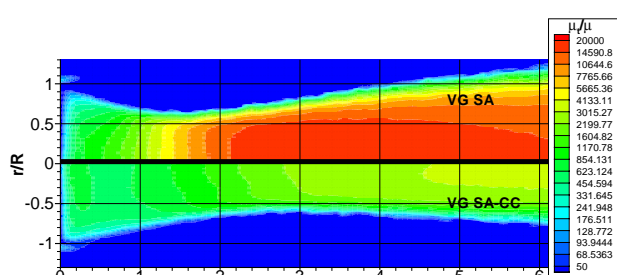


Fig. 17 Non-dimensional turbulent eddy viscosity behind the base – Spalart-Allmaras with and without compressibility corrections on VGRIDns grid

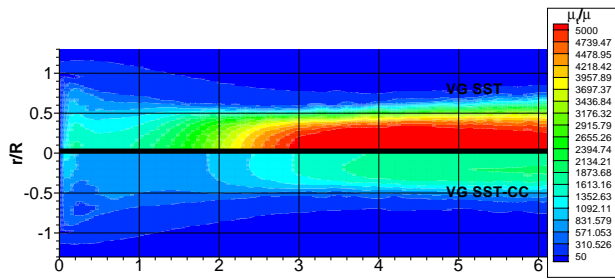


Fig. 18 Non-dimensional turbulent eddy viscosity behind the base – Shear Stress Transport with and without compressibility corrections on VGRIDns grid

file is slightly different than the experimental profile. This discrepancy was previously seen by Forsythe et al. [26] and later by Baurle et al. [29]. Baurle et al. [29] performed a calculation of the actual converging/diverging nozzle section to try to remove this discrepancy, but it made little difference.

The base pressure is next examined in Figure 11. The Spalart-Allmaras model predicts far too low of a base pressure, with a slight variation. The compressibility correction has a strong effect, putting the results much closer to the experiments, but introducing a larger variation. The SST model without the compressibility corrections does about as well as SA with the correction, and with a flatter profile. The compressibility correction then further improves the pressure level, however it again introduces more variation. The centerline velocity behind the base is next plotted in Figure 12. The SA model greatly underpredicts the shear layer reattachment location. The peak reverse velocity is overpredicted by the models with compressibility corrections, which helps to explain the increased variation in pressure along the base. Streamlines coming along the centerline towards the base stagnate on the center of the base, leading to the high pressure seen there. The Mach contours for SA with and without the corrections are compared to the experiments in Figures 13 and 14 respectively. The large reduction in turbulent eddy viscosity seen in Figure 17 has the effect of increasing the separation bubble size, which makes the turn angle at the base more realistic, but allows a larger reverse velocity, which leads to a larger variation in pressure. The SST model starts with much lower turbulent viscosity than SA, as seen in Figure 18, which allows for the larger separation bubble as seen in Figure 15. The compressibility correction further reduces the levels of eddy viscosity, increasing the size of the separation bubble further, and increasing the peak reverse velocity (Figure 16).

MILES Results

Monotone Integrated Large Eddy Simulation (MILES) uses the inherent dissipation in a numerical scheme to act as the subgrid scale model[28].

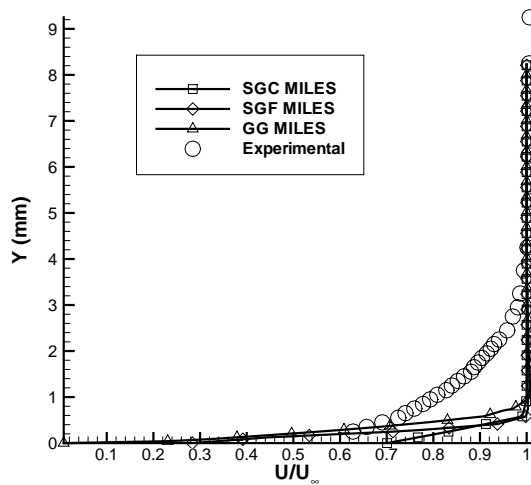


Fig. 19 Boundary layer profile 1mm prior to the base – MILES

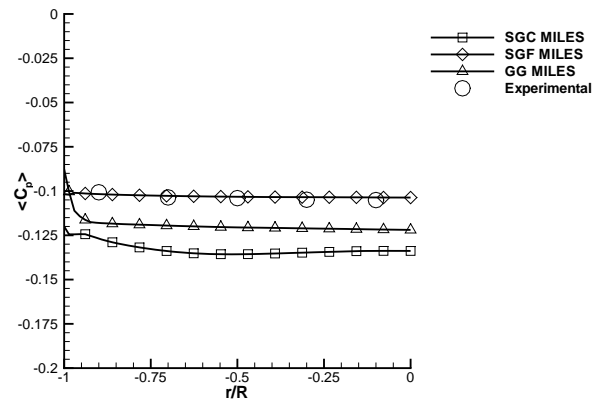


Fig. 20 Pressure along the base – MILES

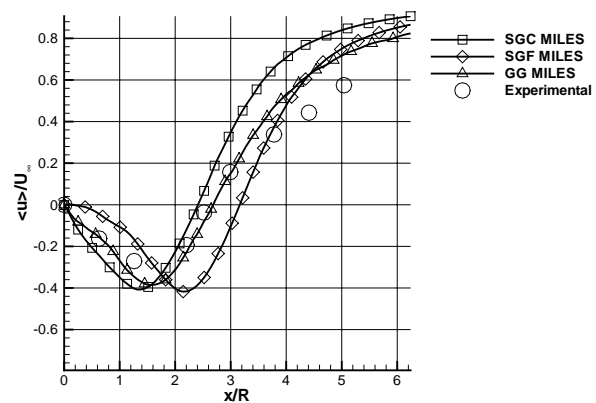


Fig. 21 Centerline velocity – MILES

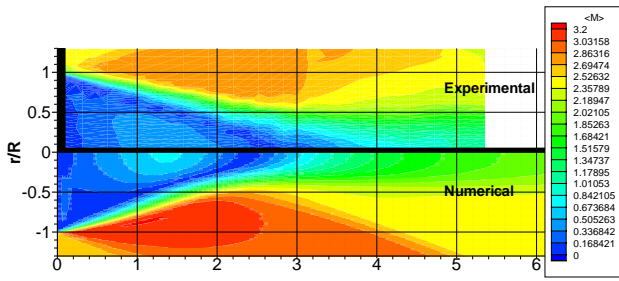


Fig. 22 Mach contours behind the base – MILES on the coarse structured grid vs. Experiments

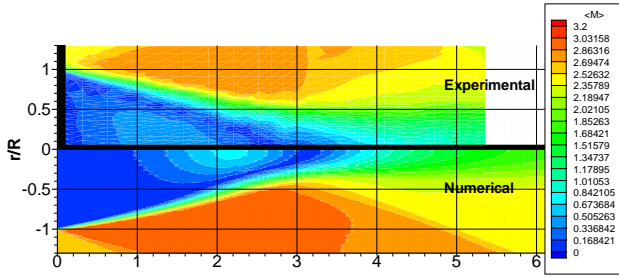


Fig. 23 Mach contours behind the base – MILES on the fine structured grid vs. Experiments

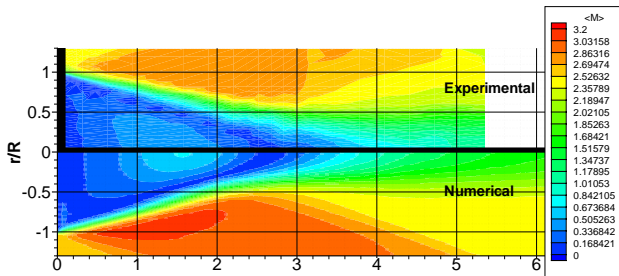


Fig. 24 Mach contours behind the base – MILES on the Gridgen grid vs. Experiments

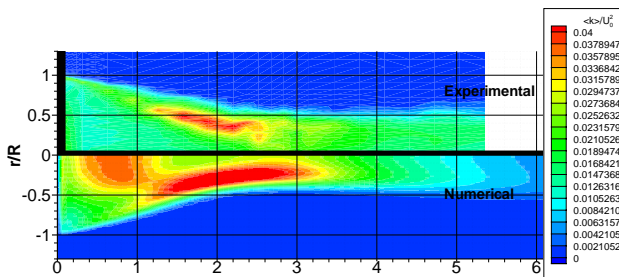


Fig. 25 Resolved turbulent kinetic energy behind the base – MILES on the coarse structured grid vs. Experiments

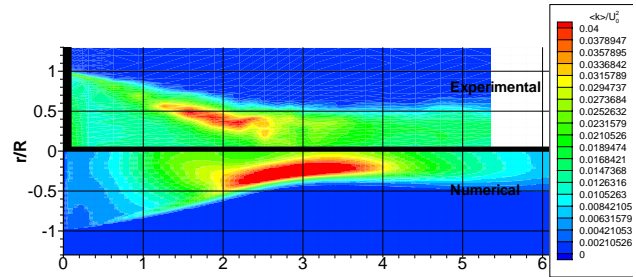


Fig. 26 Resolved turbulent kinetic energy behind the base – MILES on the fine structured grid vs. Experiments

MILES shares the same disadvantage as any subgrid scale model close to the wall, unless wall functions or a hybrid RANS/LES method is employed. To resolve rather than model the boundary layer, very fine streamwise and spanwise spacing must be used which is cost prohibitive at high Reynolds numbers. The cell spacing on the surface of the cylinder was on the order of a boundary layer thickness which is sufficient for RANS, but not LES. This resulted in an underprediction of the boundary layer thickness as seen in Figure 19. This behaviour was also seen by Fureby, Nilsson and Andersson [28] in his LES of the base flow.

The coefficient of pressure is next plotted in Figure 20. Large differences are seen as the grids are varied. All grids, however, predict a flat pressure profile as seen in the experiments. This is likely due to LES's capability to predict the unsteady flow features in contrast to RANS. The centerline velocity, shown in Figure 21 shows similar variations on the different grids. The peak reverse velocity and location, and the shear layer reattachment point are best predicted on the GG and SGC grids. The fine structured grid calculates a larger peak reverse velocity further from the base. Additionally the shear layer reattachment location is moved further downstream. In light of these discrepancies, it seems fortuitous that the fine structured grid gives the best base pressure prediction.

Mach Contours are plotted for the three grids in Figures 22 through 24. The shear layer turns too sharply for the coarse structured grid which causes the underprediction of the base pressure. The Gridgen grid exhibits the same behaviour to a lesser extent. The fine grid turns the correct amount but the shear layer remains far too thin. Looking at the resolved turbulent kinetic energy for the coarse and fine structured grids in Figures 25 and 26 may help to explain this phenomenon. The peak turbulent kinetic energy is well predicted on both grids, although at a slightly different location. k in the the shear layer is underpredicted on both grids, likely due to insufficient grid resolution or time accuracy to calculate shear layer roll up. The coarse grid actually overpredicts k directly behind the base, which is puzzling since lower resolved turbulent kinetic energy would be expected for coarser grids. A

similar behaviour as been seen by Baurle et al. [29]. A possible explanation is that the coarse grid damps out small scale structures, locking the flow into a large scale oscillation that is more energetic. Since the shear layer roll up is not resolved the only mechanism for the growth of the shear layer growth is laminar viscosity and numerical dissipation. This could explain the thin shear layer on the fine grid since the increased grid density would decrease the numerical dissipation. The fact that the boundary layer is thin to begin with adds to the error.

DES Results

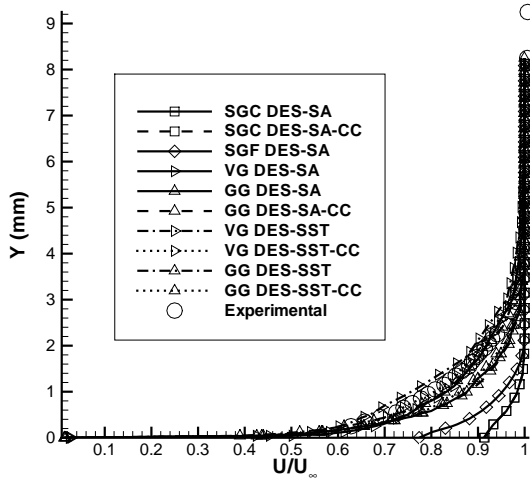


Fig. 27 Boundary layer profile 1mm prior to the base – DES

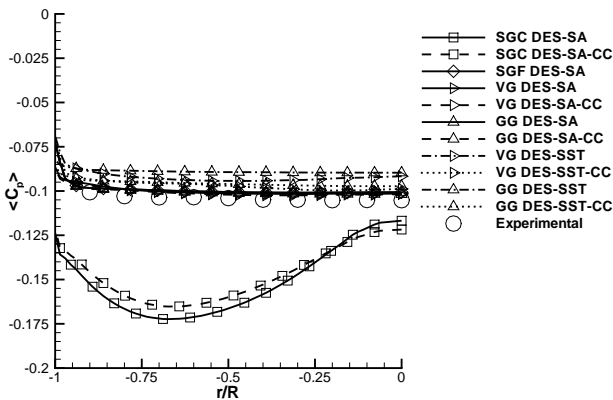


Fig. 28 Pressure along the base – DES

Boundary layer profiles for all DES runs are plotted in Figure 27. The coarse and fine structured grids fail to predict the proper boundary layer thickness due their large first y^+ values of 14 and 7 respectively. Also coarse streamwise grid spacing may have contributed to this under-prediction. All other profiles match reasonable well.

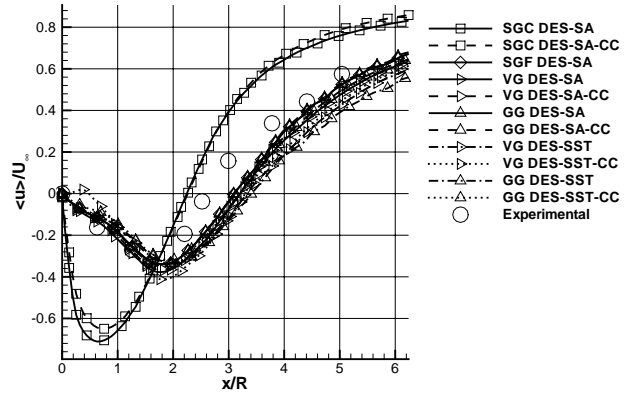


Fig. 29 Centerline velocity – DES

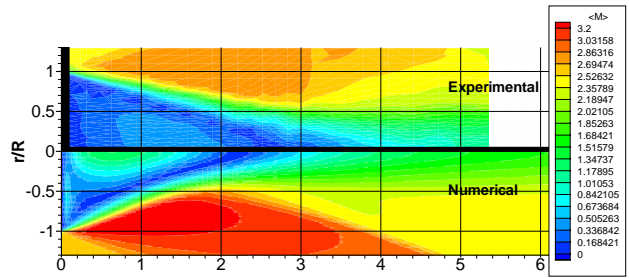


Fig. 30 Mach contours behind the base – DES Spalart-Allmaras on the coarse structured grid vs. Experiments

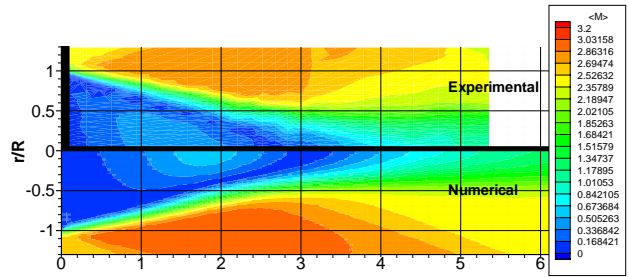


Fig. 31 Mach contours behind the base – DES Spalart-Allmaras on the fine structured grid vs. Experiments

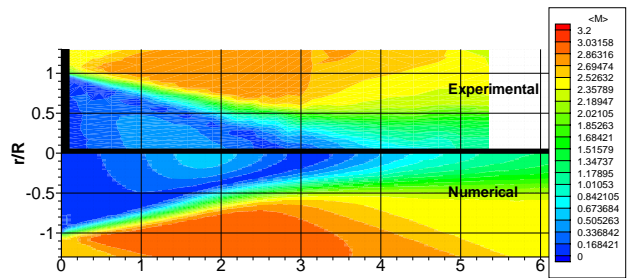


Fig. 32 Mach contours behind the base – DES Spalart-Allmaras on the Gridgen grid vs. Experiments

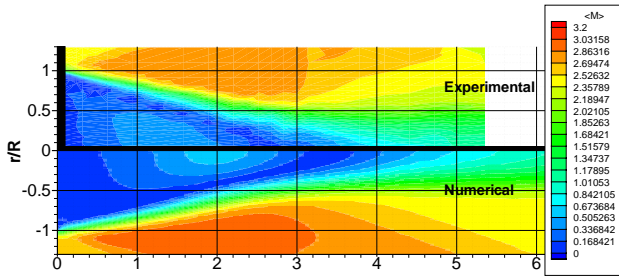


Fig. 33 Mach contours behind the base – DES Shear Stress Transport on Gridgen grid vs. Experiments

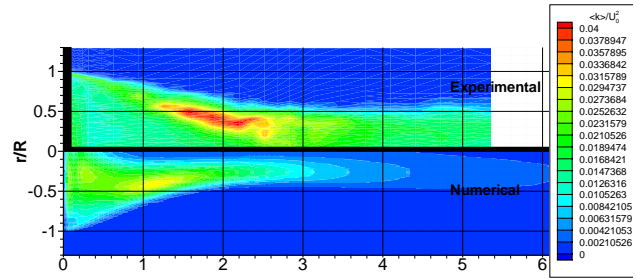


Fig. 37 Resolved turbulent kinetic energy behind the base – DES Spalart-Allmaras on the coarse structured grid vs. Experiments

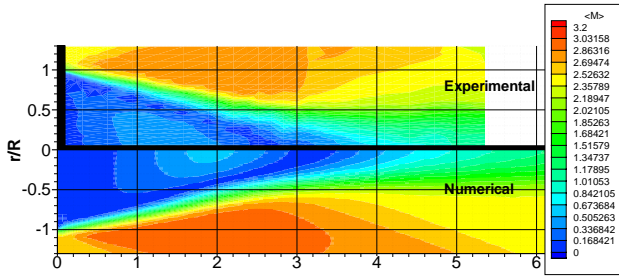


Fig. 34 Mach contours behind the base – DES Shear Stress Transport with compressibility corrections on Gridgen grid vs. Experiments

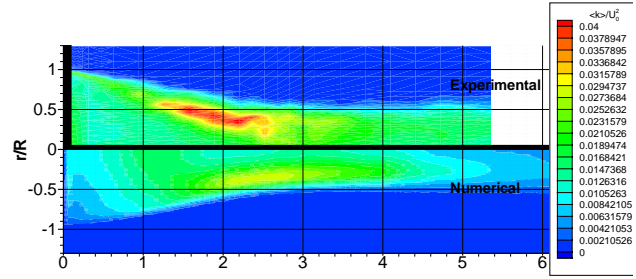


Fig. 38 Resolved turbulent kinetic energy behind the base – DES Spalart-Allmaras on the fine structured grid vs. Experiments

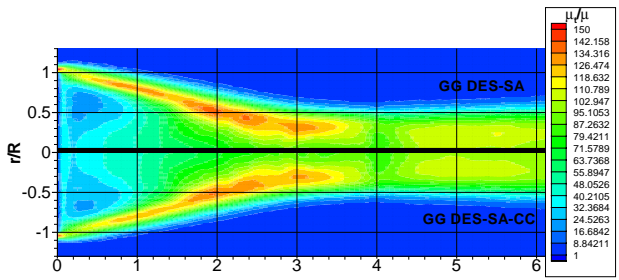


Fig. 35 Non-dimensional turbulent eddy viscosity behind the base – DES Spalart-Allmaras with and without compressibility corrections on Gridgen grid

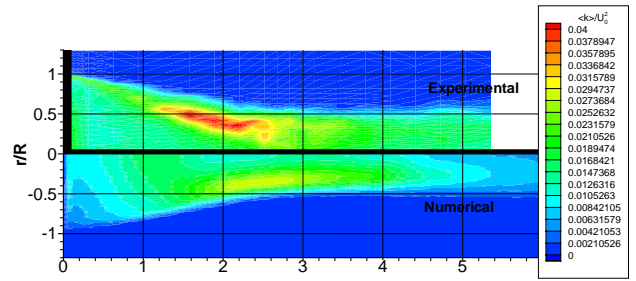


Fig. 39 Resolved turbulent kinetic energy behind the base – DES Spalart-Allmaras on the Gridgen grid vs. Experiments

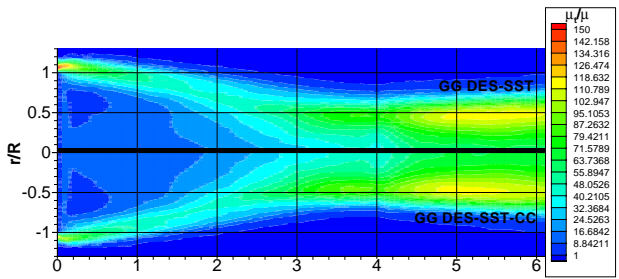


Fig. 36 Non-dimensional turbulent eddy viscosity behind the base – DES Shear Stress Transport with and without compressibility corrections on Gridgen grid

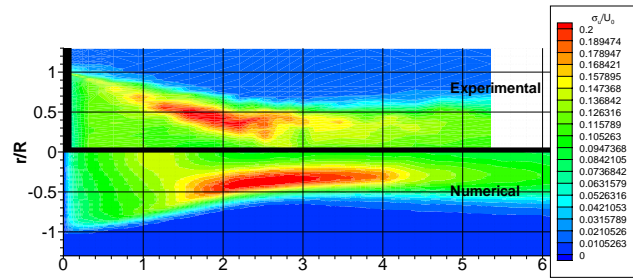


Fig. 40 Resolved streamwise turbulent intensity behind the base – DES Spalart-Allmaras on the Gridgen grid vs. Experiments

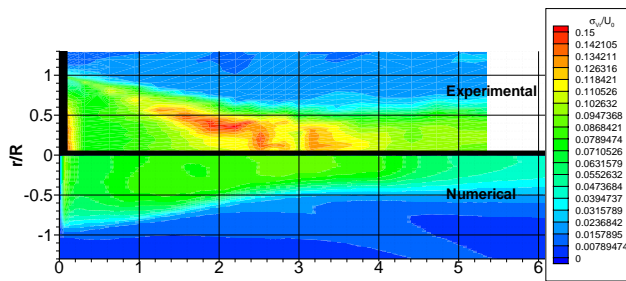


Fig. 41 Resolved radial turbulence intensity behind the base – DES Spalart-Allmaras on the Gridgen grid vs. Experiments

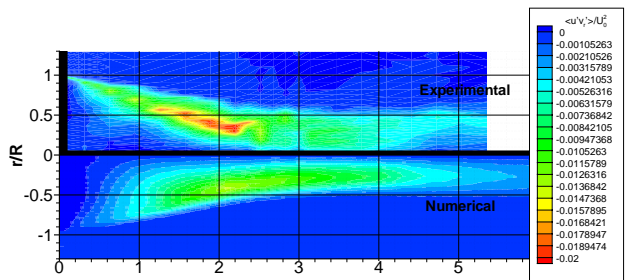


Fig. 42 Resolved Reynolds stress behind the base – DES Spalart-Allmaras on the Gridgen grid vs. Experiments

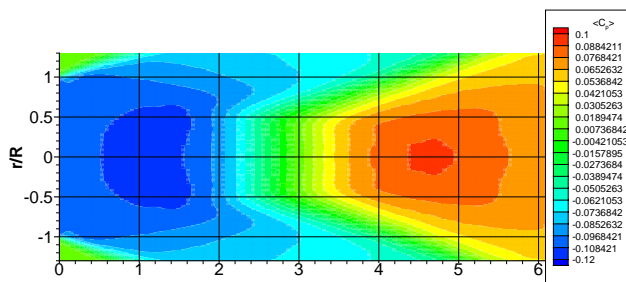


Fig. 43 Time-averaged coefficient of pressure behind the base – DES Spalart-Allmaras on the Gridgen grid

The base pressure is plotted in Figure 28. The coarse structured grid is clearly under-resolved. The compressibility correction aids the result somewhat, but not significantly. Aside from the coarse grid, the DES-SA results are remarkably insensitive to the grid or the presence of the compressibility corrections. The SST results over predict the base pressure by 5-10%, depending on the grid. The compressibility correction moves the pressure towards the experimental values.

The centerline velocity plotted in Figure 29 exhibits a similar behavior as the grid is varied. The coarse structured grid is again under-resolved, giving a high peak reverse velocity too close to the base. The fact that MILES gives a much better result for base pressure and centerline velocity on the coarse grid than DES shows that there is a significant effect of the model on this grid in addition to the numerical errors. The nature of DES is that the coarse grid limit

gives a RANS model. As the grid is refined the eddy viscosity will drop lower than a RANS prediction, yet may still be too high to allow an LES prediction.

Mach contours are compared to the experiments for various models and grids in Figures 30 through 34. Besides the coarse grid, the plots all look quite similar, even when comparing SA based DES to SST based DES. Figure 31 shows that DES is able to predict a more realistic shear layer growth than MILES on the fine grid. Plots of resolved turbulent kinetic energy (Figures 37 through 39) again suggest that the shear layer roll up is not being calculated. The shear layer growth is aided, however, by the presents of turbulent eddy viscosity as seen in Figures 35 and 36. The turbulent kinetic energy is underpredicted on all grids (Figures 37 through 39), especially in the shear layer. Grid refinement should enhance the agreement to the experiments, but since some turbulence is still being modelled (especially in the shear layer), the mean flow properties are reasonable.

Figures 39 through 42 plot turbulent statistics for DES-SA on the Gridgen grid. Although underpredicting the statistics in general, the agreement is fair. The resolved radial turbulence intensity is furthest from the experiments. A plot of pressure coefficient behind the base is shown in Figure 43, although there is no experimental data to compare it to. The constant pressure region behind the base is evident, as well as the reattachment shock that forms at $x/R = 3.0$.

Conclusion

A detailed testing of DES based on both the Spalart-Allmaras and the Shear Stress Transport model was conducted on the supersonic axisymmetric base of Herpin and Dutton [8]. Comparisons were made to the Spalart Allmaras and Shear Stress Transport RANS modes as well as LES. Compressibility corrections were examined for the RANS and DES models.

Both the SA and the SST RANS models seem "flawed" to begin with for this flow. Mach contours for both models are in significant disagreement with the experiments. Compressibility corrections aid the models in predicting a more realistic level of pressure on the base, but increase the variation of the pressure due to the increased centerline velocity. LES, in contrast, predicts a flat pressure profile due to its ability to model the unsteady flow that helps equalize the base pressure. LES has problems predicting the shear layer growth for the current simulations. This error could potentially be reduced by resolving the shear layer instabilities. The error in predicting the boundary layer thickness would be far more challenging to fix, since at these high Reynolds number the boundary layer is thin and would require an excessively fine grid and small timestep to resolve. DES predictions successfully predicted the boundary layer thickness prior to the base, while retaining LES's ability to predict the

flat base pressure profile.

Calculations were performed on two structured and two unstructured grids to examine the effect of grid resolution and topology. The DES calculations seemed less sensitive to grid changes than DES, although the coarse grid LES solution was superior to the DES solution on that grid. Spalart Allmaras based DES predicted the base pressure to within a few percent on all but the coarse grid. SST based DES predicted higher pressures than the experiments (worst disagreement was 10%). Compressibility corrections helped improve the agreement with base pressure for the SST based DES, however the turbulent eddy viscosity contours were so similar it is difficult to understand the reason for the improvement. Compressibility corrections had a negligible impact on Spalart-Allmaras based DES. Unstructured gave solutions that agreed well with structured grids and the experiments.

Acknowledgments

Computer time was provided by the Maui High Performance Computing Center and the NAVO Major Shared Resource Center. Dr. Spalart provided some very helpful discussions and originally motivated this work. Dr. Strelets provided results from other runs to ensure that the Spalart-Allmaras model was coded correctly. Bill Strang of Cobalt Solutions coded the compressibility corrections to Spalart-Allmaras model as well as many other features that made this study possible. Dr. Dutton provided the experimental data.

References

- ¹ Spalart, P. R., "Strategies for Turbulence Modeling and Simulations," 4th Int. Symp. Eng. Turb. Modelling and Measurements, Corsica, May 24-26, 1999.
- ² Spalart, P. R., Jou W-H., Strelets M., and Allmaras, S. R., "Comments on the Feasibility of LES for Wings, and on a Hybrid RANS/LES Approach," *Advances in DNS/LES, 1st AFOSR Int. Conf. on DNS/LES*, Aug 4-8, 1997, Greyden Press, Columbus Oh.
- ³ Shur, M., Spalart, P. R., Strelets, M., and Travin, A., "Detached-Eddy Simulation of an Airfoil at High Angle of Attack, 4th Int. Symp. Eng. Turb. Modelling and Measurements, Corsica, May 24-26, 1999.
- ⁴ Constantinescu, G.S., Squires, K.D., "LES and DES Investigations of Turbulent Flow over a Sphere," *AIAA 00-0540*, Jan 2000.
- ⁵ Travin, A., Shur, M., Strelets, M., and Spalart, P.R., "Detached-Eddy Simulation Past a Circular Cylinder," *Int. J. Flow, Turbulence and Combustion*, 2000, V.63, Nos. 1-4, pp. 293-313.
- ⁶ Strelets, M., "Detached Eddy Simulation of Massively Separated Flows," *AIAA 01-0879*, Jan 2001.
- ⁷ Forsythe, J.R., Hoffmann, K.A., Dieteker, F.-F., "Detached-Eddy Simulation of a Supersonic Axisymmetric Base Flow with an Unstructured Flow Solver," *AIAA 00-2410*, June 2000.
- ⁸ Herrin, J. L., Dutton, J. C., "Supersonic Base Flow Experiments in the Near Wake of a Cylindrical Afterbody," *AIAA Journal*, Vol. 32, No1, Jan 1994.
- ⁹ Herrin, J.L., Dutton, J.C., "Supersonic Base Flow Experiments in the Near-Wake of a Cylindrical Afterbody," *AIAA 93-2924*, July 1993.
- ¹⁰ Bourdon, C.J., Smith, K.M., Dutton, M., Mathur, T., "Planar Visualizations of Large-Scale Turbulent Structures in Axisymmetric Supersonic Base Flows," *AIAA 98-0624*, Jan 1998.
- ¹¹ Dutton, J.C., Herrin, J.L., Molezzi, M.J., Mathur, T., Smith, K.M., "Recent Progress on High-Speed Separated Base Flows," *AIAA 95-0472*, Jan 1995.
- ¹² Goebel, S.G., Dutton, J.C., "Experimental Study of Compressible Turbulent Mixing Layers," *AIAA Journal*, Vol. 29, No. 4, pp. 538-546. 1991.
- ¹³ Clemens, N.T., and Mungal, M.G., "Two- and Three-Dimensional Effects in the Supersonic Mixing Layer," *AIAA Journal*, Vol. 30, No. 4, pp. 973-981, 1992.
- ¹⁴ Delery, J. and Lacau, R.G., "Prediction of Base Flows," *AGARD Report 654*, 1987.
- ¹⁵ Putnam, L.E., and Bissinger, N.C., "Results of AGARD Assessment of Prediction Capabilities for Nozzle Afterbody Flows," *AIAA 85-1464*. 1095.
- ¹⁶ Petrie, H.L., and Walker, B.J., "Comparison of Experiment and Computation for a Missile Base Region Flowfield with a Centered Propulsive Jet," *AIAA 85-1618*, 1985.
- ¹⁷ Benay, R., Coet, M.C., and Delery, J., "Validation of Turbulence Models Applied to Transonic Shock-Wave/Boundary-Layer Interaction," *La Recherche Aeronautique*, No. 1987-3, pp. 1-16, 1987.
- ¹⁸ Caruso, S.C., and Childs, R.E., "Aspects of Grid Topology for Reynolds-Averaged Navier-Stokes Base Flow Computations," *AIAA 88-0523*, 1988.
- ¹⁹ Childs, R.E. and Caruso, S.C., "On the Accuracy of Turbulent Base Flow Predictions," *AIAA 87-1439*, 1987.
- ²⁰ Childs, R.E. and Caruso, S.C., "Assessment of Modeling and Discretization Accuracy for High Speed Afterbody Flows," *AIAA 89-0531*, 1989.

- ²¹ Peace, A.J., "Turbulent Flow Predictions for Afterbody/Nozzle Geometries Including Base Effects," *Journal of Propulsion and Power*, Vol. 24, No. 3, pp. 396—403, 1991.
- ²² Tucker, P.K., and Shyy, W., "A Numerical Analysis of Supersonic Flow Over an Axisymmetric Afterbody," *AIAA 93-2347*, 1993.
- ²³ Suzen, Y.B., Hoffmann, K.A., Forsythe, J.R., "Application of Several Turbulence Models for High Speed Shear Layer Flows." *AIAA 99-0933*, Jan 1999.
- ²⁴ Sahu, J., "Numerical Computations of Supersonic Base Flow with Special Emphasis on Turbulence Modeling," *AIAA Journal*, Vol. 32, No. 7, pp 1547—1549, 1994.
- ²⁵ Chuang, C.C., Chieng, C.C., "Supersonic Base Flow Computations by Higher Order Turbulence Models," *Journal of Spacecraft and Rockets*, Vo. 33, No. 3, 1996.
- ²⁶ Forsythe, J.R., Strang, W., Hoffmann, K.A., "Validation of Several Reynolds-Averaged Turbulence Models in a 3D Unstructured Grid Code," *AIAA 00-2552*, June 2000.
- ²⁷ Harris, P.J., Fasel, H.F., "Numerical Investigation of the Unsteady Behavior of Supersonic Plane Wakes," *AIAA 98-2947*, 1998.
- ²⁸ Fureby, C., Nilsson, Y., Andersson, K., "Large Eddy Simulation of Supersonic Base Flow," *AIAA 99-0426*, Jan 1999.
- ²⁹ Baurle, R. A., Tam, C.-J., Edwards, J. R., Hassan, H. A., "An Assessment of Boundary Treatment and Algorithm Issues on Hybrid RANS/LES Solution Strategies," *AIAA 01-*.
- ³⁰ Strang, W. Z., Tomaro, R. F., Grismer, M. J., "The Defining Methods of Cobalt₆₀: a Parallel, Implicit, Unstructured Euler/Navier-Stokes Flow Solver," *AIAA 99-0786*, January 1999.
- ³¹ Tomaro, R.F., Strang, W. Z., and Sankar, L. N., "An Implicit Algorithm for Solving Time Dependent Flows on Unstructured Grids," *AIAA 97-0333*, January 1997.
- ³² Grismer, M. J., Strang, W. Z., Tomaro, R. F. and Witzeman, F. C., "Cobalt: A Parallel, Implicit, Unstructured Euler/Navier-Stokes Solver," *Advances in Engineering Software*, Vol. 29, No. 3-6, pp. 365—373, 1998.
- ³³ Karypis, G., and Kumar, V., *METIS: Unstructured Graph Partitioning and Sparse Matrix Ordering System Version 2.0*. University of Minnesota, Department of Computer Science, Minneapolis, MN 55455, July 1997.
- ³⁴ Karypis, G., Schloegel, K., and Kumar, V, *ParMETIS: Parallel Graph Partitioning and Sparse Matrix Ordering Library Version 1.0*. University of Minnesota, Department of Computer Science, Minneapolis, MN 55455, July 1997.
- ³⁵ Mathur, T., Dutton, J.C., "Base Bleed Experiments with a Cylindrical Afterbody in Supersonic Flow," *AIAA 95-0062*, 1995.
- ³⁶ Spalart, P. R., and Allmaras, S. R., "A One-Equation Turbulence Model for Aerodynamic Flows," *AIAA-92-0439*, Jan 1992.
- ³⁷ Spalart, P. R., "Trends in Turbulence Treatments," *AIAA 00-2306*, July 2000.
- ³⁸ Shur, M., Strelets, M., Zaikov, L., Gulyaev, A., Kozlov, V., and Secundov, A., "Comparative Numerical Testing of One- and Two- Equation Turbulence Models for Flows with Separation and Reattachment," *AIAA 95-0863*.
- ³⁹ Menter, F.R., "Influence of Freestream Values on $k-\omega$ Turbulence Model Predictions," *AIAA Journal*, Vol 30, No 6, 1991, pp 1657—1659.
- ⁴⁰ Menter, F.R., "Improved Two-Equation $k-\omega$ Turbulence Models for Aerodynamic Flows," *NASA-TM-103975*, October 1992.
- ⁴¹ Menter, F.R., "Zonal Two Equation $k-\omega$ Turbulence Models for Aerodynamic Flows," *AIAA 93-2906*, 1993.
- ⁴² Menter, F.R., "Two-Equation Eddy-Viscosity Turbulence Models for Engineering Applications," *AIAA Journal*, Vol 32, No 8, August 1994, pp 1598—1605.
- ⁴³ Suzen, Y. B., Hoffmann, K. A., "Investigation of Supersonic Jet Exhaust Flow by One- and Two-Equation Turbulence Models," *AIAA 98-0322*, January 1998.
- ⁴⁴ Forsythe, J.R., Hoffmann, K.A., Suzen, Y.B., "Investigation of Modified Menter's Two-Equation Turbulence Models for Supersonic Applications." *AIAA 99-0873*, January 1999.
- ⁴⁵ Wilcox D.C., *Turbulence Modeling for CFD*, Second Edition, DCW Industries, Inc., 1998.
- ⁴⁶ Pirzadeh, S., "Three-dimensional Unstructured Viscous Grids by the Advancing Layers Method," *AIAA Journal*, V. 34, pp. 43-49.
- ⁴⁷ Steinbrenner, J., Weyman, N., Chawner, J., "Development and Implementation of Gridgen's Hyperbolic PDE and Extrusion Methods," *AIAA 00-0679*, January 2000.
- ⁴⁸ Spalart, P., "Young-Person's Guide to Detached-Eddy Simulation Grids," *NASA CR 2001-211032*.